WAVEFRONT TOMOGRAPHY WITH ENFORCED DIFFRACTION FOCUSING

A. Bauer, B. Schwarz, L. Diekmann, and D. Gajewski

email: *alex.bauer@uni-hamburg.de*

keywords: *diffraction, focusing, tomography, wavefront, inversion*

ABSTRACT

Wavefront tomography is an efficient and stable tool for the generation of smooth velocity models. As input it requires first and second-order attributes, which describe slope and curvature of the measured wavefronts. These wavefront attributes can be extracted from the data by multi-parameter stacking schemes such as the common-reflection-surface (CRS) stack. While the slopes are stable and relatively easy to determine, the wavefront curvatures can become unreliable in the case of sparsely-sampled data or strong lateral heterogeneity. Since wavefront tomography is mainly driven by the misfit of modeled and measured wavefront curvatures, curvatures of bad quality may compromise its convergence. A possible solution to overcome this problem are diffractions, which have a unique property that can be exploited for better constraining the inversion: all measurements belonging to the same diffracted event are connected to the same subsurface structure, although registered at different positions on the recording surface. In recent work, we introduced an event-tagging scheme that automatically assigns a unique tag to each diffraction in the data. We propose to use this information to constrain the inversion by enforcing all diffracted measurements with the same tag to focus in depth, thus overcoming the sole dependency of wavefront tomography on second-order attributes. Results for diffraction-only data with vertical and lateral heterogeneity confirm that it is possible to obtain depth velocity models for zero-offset data without using curvature information and that the suggested approach may help to increase the stability of wavefront tomography in complex settings.

INTRODUCTION

While traditional seismic imaging has often been designed to favor reflections, the true potential of the weak diffracted wavefield has rarely been recognized (Krey, 1952). In the last two decades, however, diffractions have gained importance and numerous applications have been proposed (e.g. Landa and Keydar, 1998; Fomel et al., 2007; Moser and Howard, 2008; Klokov and Fomel, 2012; Bauer et al., 2016, 2017; Schwarz, 2019). The main motivation for this change of mind is the fact that seismic diffractions occur at small-scale subsurface structures, which are often related to interesting geological features such as faults and pinch-outs and thus contain high-resolution information about the subsurface (Khaidukov et al., 2004). Since Snell's law does not hold for diffractions, any seismic diffraction can be recorded at various positions of the recording surface, which implies a better illumination of the subsurface compared to reflected waves.

In the recent years, wavefront attributes – initially being a by-product of multi-parameter stacking schemes such as the common-reflection-surface stack (CRS, Jäger et al., 2001) – have proven to be a powerful tool for seismic data analysis. While they are physical properties of hypothetical wavefronts in the reflection case, for diffractions they describe the actual wavefronts. Wavefront attributes can not only be used for imaging (e.g. Eisenberg-Klein et al., 2008; Baykulov and Gajewski, 2009; Dell and Gajewski, 2011; Bauer et al., 2016; Walda and Gajewski, 2017; Schwarz and Gajewski, 2017; Schwarz, 2019), but also for velocity model building with wavefront tomography (Duveneck, 2004). Recently, we have shown that the unique physical properties of diffractions can help to improve the resolution of depth velocity

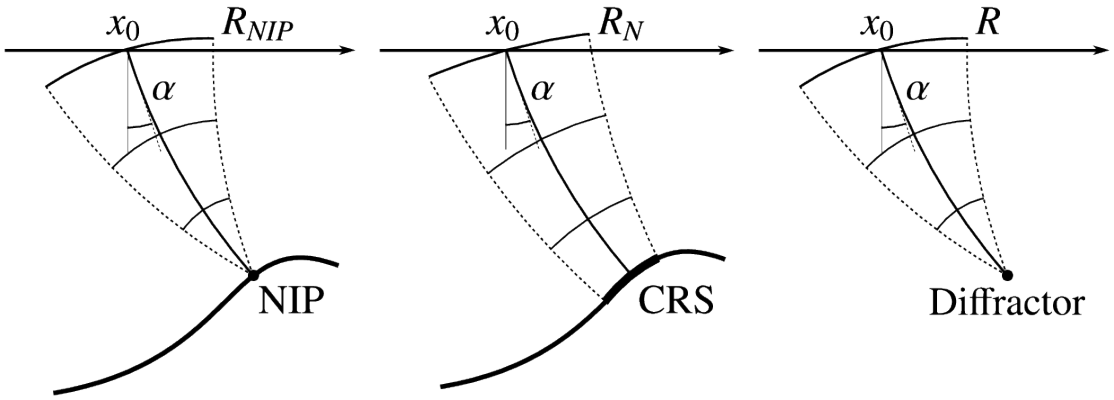

(a) Reflection case: NIP wave **(b)** Reflection case: normal wave **(c)** Diffraction case

Figure 1: The 2D wavefront attributes α, R_{NIP} and R_N. In the general reflection case, the NIP wave (left) is excited by a point source placed on the reflector's point of normal incidence (NIP) and the normal wave (middle) is excited by an exploding reflector segment (CRS) around the NIP. In the case of a diffraction (right), the exploding reflector segment shrinks to a point that is the actual diffractor acting as a secondary source. As a result, R_{NIP} and R_N coincide and the NIP wave is no longer fictitious, but it describes the actual diffracted wavefront.

models obtained with wavefront tomography (Bauer et al., 2017). A drawback of existing techniques for velocity-model building such as stereotomography (Billette and Lambaré, 1998), its successor adjoint slope tomography (Tavakoli F et al., 2017) or full-waveform inversion (e.g. Virieux and Operto, 2009) is that these methods require seismic data with sufficiently large offsets. However, the acquisition of seismic data with large offsets is expensive and merely feasible for the hydrocarbon industry, while academic institutions often have to cope with low-cost acquisitions and short streamers. Owing to their focusing nature, we argue that diffractions may serve as a solution to overcome this problem. However, a requirement for further benefitting from the properties of diffractions is the identification of measurements connected to the same diffraction – and thus the same subsurface structure – in the data. For this purpose, we recently proposed a scheme, which utilizes the local similarity of zero-offset wavefront attributes to globally assign tags to every diffraction in a zero-offset section (Bauer et al., 2019). While every data point is treated independently in conventional wavefront tomography, the availability of these event tags allows for both event-consistent statistics, that is, quality control or uncertainty analysis of the obtained velocity models (Bauer et al., 2019), and further constraining the inversion algorithm by enforcing diffraction focusing in depth.

In this work, we introduce diffraction wavefront tomography, a modified implementation of wavefront tomography, in which all diffractions with the same tag are forced to focus in depth. As a by-product, this new constraint reduces the dependency of wavefront tomography on the curvature-related second-order wavefront attributes. If curvatures are not taken into account at all, the new method evolves into a zero-offset slope tomography for diffractions. This allows its application to data, in which the determination of curvatures is challenging, such as settings with strong lateral heterogeneity or zero-offset data with few traces. Applications to synthetic diffraction data with vertical and lateral heterogeneity confirm the potential of the modified implementation, which is likewise applicable to passive seismic data (Diekmann et al., 2019).

WAVEFRONT ATTRIBUTES

The input for the inversion algorithm used in this work are the so-called zero-offset wavefront attributes (Hubral, 1983), which can be determined via multi-parameter stacking schemes such as the common-reflection-surface stack (CRS, Jäger et al., 2001). The wavefront attributes are encoded in the first and

second derivatives of the traveltime moveout Δt given by

$$\Delta t^2(t_0, x_0) = (t_0 + 2p\Delta x)^2 + 2t_0(M_{NIP}h^2 + M_N\Delta x^2) \,, \tag{1}$$

where t_0 is the zero-offset time sample under consideration, $\Delta x = x - x_0$ is the distance from the central midpoint x_0 and h is the half-offset. The first derivative of Δt is the horizontal slowness p that can be expressed in terms of the emergence angle α of the wavefront measured at the recording surface,

$$p = \frac{\sin\alpha}{v_0} \,, \tag{2}$$

where v_0 denotes the near-surface velocity. The second-order quantities M_{NIP} and M_N can be parametrized by the radii of two fictitious wavefronts, R_{NIP} and R_N,

$$M_{NIP} = \frac{\cos^2\alpha}{v_0 R_{NIP}} \,, \qquad M_N = \frac{\cos^2\alpha}{v_0 R_N} \,. \tag{3}$$

In the general case of a seismic reflection, R_{NIP} is the radius of a wavefront excited by a hypothetical point source placed on the reflector's point of normal incidence (NIP, compare Figure 1(a)) and R_N is the radius of a wavefront excited by an exploding reflector segment around the NIP (Figure 1(b)). Consequently, R_{NIP} is related to the depth of a reflector and R_N is related to its curvature. However, in the case of a diffraction, the point source is no longer hypothetical, but it is the diffractor acting as a secondary source, and the reflector segment reduces to the NIP (Figure 1(c)). Therefore, R_{NIP} and R_N coincide for diffractions and the NIP wave is the actual wavefront measured at the recording surface. Hence, in contrast to the reflection case, where offsets in the data are required for the estimation of wavefront attributes, diffraction wavefront attributes can also be determined for zero-offset data. Moreover, note that the moveout of a passive seismic event can be described by the same quantities, except for the additionally unknown source excitation time, as the moveout of an active seismic diffraction (Schwarz et al., 2016). As a result, the inversion scheme presented in this work is equally applicable to passive seismic data (Diekmann et al., 2019). While the first-order slopes p in general are easy to extract from the data, the determination of second-order curvatures, that is M_{NIP} and M_N, is more challenging. Particularly in complex settings with a laterally heterogeneous subsurface the successful determination of curvatures strongly depends on the chosen aperture.

The results of the CRS stack, namely a zero-offset section with improved signal-to-noise ratio, a coherence section and the wavefront attributes p and M_{NIP}, are a prerequisite for the application of wavefront tomography, which we will introduce in the following.

WAVEFRONT TOMOGRAPHY

Wavefront tomography is an efficient and stable method for the determination of smooth depth-velocity models. In the following, we will shortly describe conventional wavefront tomography (Duveneck, 2004), which can be applied to both reflections and diffractions (Bauer et al., 2017). Afterwards, we will introduce a modified implementation of wavefront tomography for diffraction-only data, in which diffractions are forced to focus in depth.

Conventional approach

As input for wavefront tomography, data points $\mathbf{d}_i$ have to be picked in the zero-offset sections. This can be done in an automatic fashion based on the semblance value associated to the measurements,

$$\mathbf{d}_i = (x_0, T, p, M_{NIP})_i \,, \qquad i = 1, \ldots, n_{picks} \,, \tag{4}$$

where x_0 is the midpoint coordinate and $T = t_0/2$ is the one-way zero-offset traveltime. The velocity model is defined in terms of 2D B-splines,

$$v(x, z) = \sum_{k=1}^{n_x} \sum_{l=1}^{n_z} v_{kl}\beta_k(x)\beta_l(z) \,, \tag{5}$$

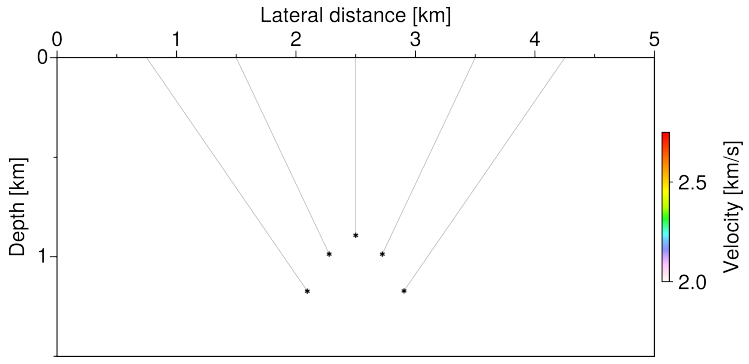

Figure 2: Illustration of five initial ray paths of conventional wavefront tomography for a simple data example with one diffraction. The ray paths of the downward and upward ray tracing coincide. As a result, the initial misfit only depends on M_{NIP}.

where n_x and n_z are the number of knots in x- and z direction, respectively, and v_{kl} are the velocity values at the corresponding locations. Accordingly, the model space $\mathbf{m}$ is defined by the $n_x \times n_z$ B-spline velocity coefficients, subsurface locations $(x, z)_i$ and ray take-off angles θ_i associated to each data point. In the inversion algorithm, downward kinematic ray tracing into the given initial velocity model yields first guesses of the localizations $(x, z)_i$ of each data point. As a next step, upward dynamic ray tracing starting from $(x, z)_i$ provides the modeled data $\tilde{\mathbf{d}}$. After the initial modeling, due to the reciprocity of downward und upward ray paths, the modeled attributes $\tilde{\mathbf{d}}$ and the measured attributes $\mathbf{d}$ only differ in the values of M_{NIP}, which are calculated during the dynamic ray tracing. Figure 2 illustrates five ray paths of the initial modeling for a simple diffraction example. Due to the wrong initial model, the localizations $(x, z)_i$ of the five data points, which would coincide in a correct velocity model, still form a hyperbola. For the inversion scheme, the misfit between measured and modeled data $\Delta\mathbf{d} = \mathbf{d} - \tilde{\mathbf{d}}$ is defined in terms of a cost function

$$\Psi(\mathbf{m}) = \frac{1}{2}\|\mathbf{d} - \tilde{\mathbf{d}}\|_2^2 + \Lambda\left(\partial_{xx}v(x,z)), \partial_{zz}v(x,z)\right) \ , \tag{6}$$

which is minimized in a least-squares sense by an LSQR algorithm (Paige and Saunders, 1982). The second term Λ of the cost function is responsible for regularization and ensures a smooth velocity model by minimizing its second derivatives. For more details on the iterative solution of the inverse problem we refer to the original work of Duveneck (2004). In order to account for the different units of the attributes (x_0, T, p, M_{NIP}), they are weighted with given factors (w_x, w_T, w_p, w_M) that have to be chosen by the user depending on the attribute quality and the problem at hand. However, since the initial misfit of conventional wavefront tomography only depends on the values of M_{NIP}, the weighting factor w_M must not be set to zero. Consequently, in complex settings, where the estimation of second-order attributes is challenging, this may lead to an unstable behavior of the inversion scheme.

Diffraction wavefront tomography

While in conventional wavefront tomography all data points are treated independently, diffractions allow the introduction of an additional constraint into the algorithm: all data points that belong to the same diffraction are connected to the same subsurface structure and therefore, all localizations connected to the same diffraction have to focus in depth. However, the implementation of this constraint requires the previous identification and tagging of diffractions, such that a unique identifier, that is, an *event tag*, is assigned to every diffraction present in the data. Bauer et al. (2019) recently introduced a scheme that identifies and tags diffractions in an unsupervised fashion by analyzing the local similarity of wavefront attributes.

Accordingly, the diffraction wavefront tomography we propose requires an additional input parameter: the event tag associated with each data point. The data space $\mathbf{d}$ is then given by

$$\mathbf{d}_i = (x_0, T, p, M_{NIP}, j)_i \ , \qquad i = 1, \ldots, n_{picks} \ , \qquad j = 1, \ldots, n_{events} \ , \tag{7}$$

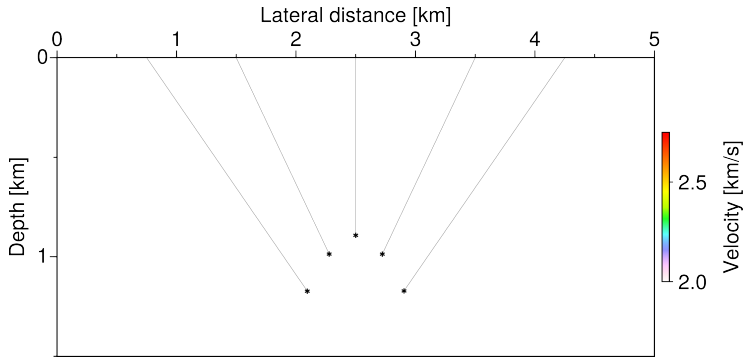

(a) Downward ray paths

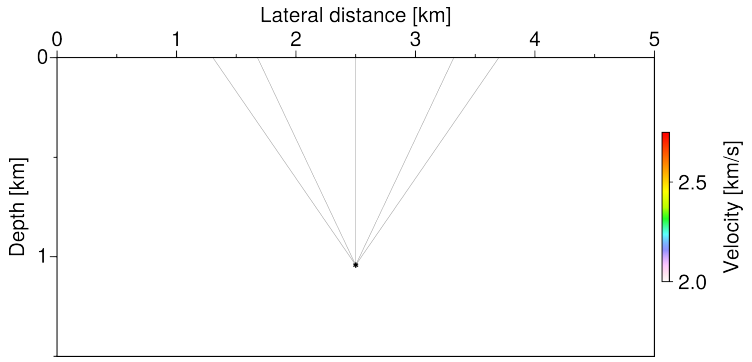

(b) Upward ray paths

Figure 3: Illustration of five initial ray paths of diffraction wavefront tomography for a simple data example with one diffraction. The ray paths of the (a) downward and (b) upward ray tracing differ, because all localizations are set to their mean value after the downward ray tracing. As a result, the initial misfit mainly depends on x_0 and T.

where j denotes the event tag and n_{events} is the number of different diffractions identified in the data. As in the original implementation, the first step of the initial modeling consists of downward kinematic ray tracing into the initial velocity model, which yields first guesses of the subsurface locations $(x, z)_i$ related to each data point. These initial downward ray paths are illustrated in Figure 3(a). While in the original implementation upward dynamic ray tracing starting from $(x, z)_i$ with the take-off angles θ_i provides the modeled data $\tilde{\mathbf{d}}$, in our modified implementation, the mean subsurface locations of all data points with the same event tag $(\bar{x}, \bar{z})_j$ are calculated and the upward dynamic ray tracing is started from these locations. In this case, the ray take-off angles are calculated from the measured slowness values p_i. The resulting initial upward ray paths for the simple diffraction example are illustrated in Figure 3(b). Since they differ from the downward ray paths, this results in an initial misfit $\Delta\mathbf{d}$, which does not only depend on M_{NIP}, but mainly on x_0 and T. Consequently, the modified implementation allows setting the weighting factor w_M to zero, thereby evolving into a zero-offset slope tomography for diffractions.

DATA EXAMPLES

In this section, we present synthetic data examples comparing diffraction wavefront tomography to the conventional approach and analyzing the stability of the proposed method in the presence of lateral heterogeneity.

Simple diffraction data with vertical heterogeneity

The first example consists in an application of both conventional wavefront tomography and our modified implementation to synthetic diffraction data obtained in a vertically inhomogeneous velocity model with

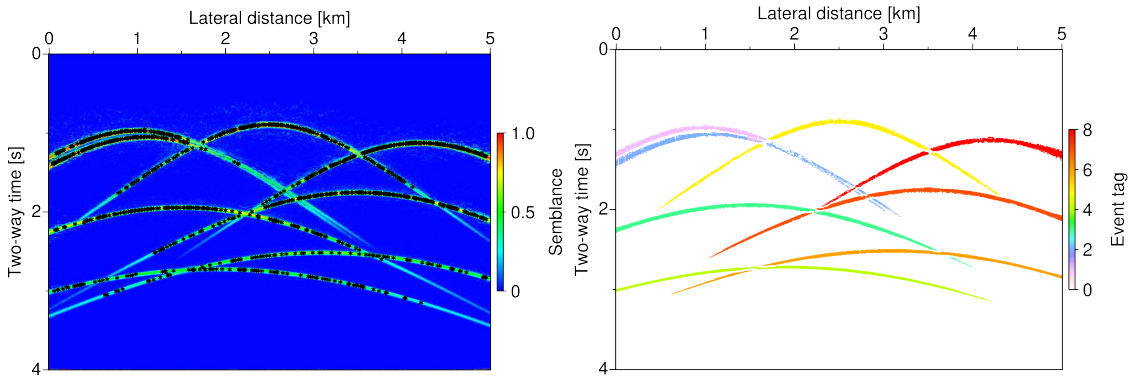

(a) Picked data points **(b)** Initial model

Figure 4: Panel (a) shows the automatically picked data points plotted onto the zero-offset semblance, (b) the event tags obtained in an automatic fashion.

a velocity gradient of $0.5\,\mathrm{s}^{-1}$. The dataset contains a total of eight point diffractors. The input for the inversion, 879 automatically picked data points, is displayed in Figure 4(a) plotted onto the zero-offset semblance section provided by the CRS stack. Figure 4(b) shows the event tags that have been obtained in an unsupervised fashion based on the local similarity of the corresponding wavefront attributes (Bauer et al., 2019). The inversion results are presented in Figure 5. In the upper row, the results of conventional wavefront tomography are shown: starting from a constant initial model, displayed in Figure 5(a), consisting in the near-surface velocity v_0 with the initial localizations (black asterisks) connected to all data points, the inversion algorithm converged to the final model displayed in Figure 5(b) with the final localizations. Figure 5(c) shows the constant initial model of diffraction wavefront tomography with the initial scatterer localizations $(\bar{x}, \bar{z})_j$ connected to each event tag (black dots). For all inversion runs, an initial grid of 6×5 B-spline knots with a spacing of 1000 m each was used. In a cascaded approach, the knot spacing was halved three times during the inversions, thus ending up with a 41×33-grid with a spacing of 125 m each. While Figure 5(b) is the result obtained with conventional wavefront tomography, Figures 5(d) and 5(e) are the models obtained with our modified implementation. In the latter, we set the weight for the curvatures w_M to zero, that is, no curvature information was used in the inversion. While this would imply a vanishing misfit and no convergence in the original implementation, in the modified implementation this approach provides a result of at least the same quality as the conventional implementation compared to the correct model (Figure 5(f)). Still, for this dataset without lateral heterogeneity it is possible to obtain good results with both implementations and both with or without relying on curvature information in diffraction wavefront tomography.

Simple diffraction data with lateral and vertical heterogeneity

The results for the second example, presented in Figure 6, are based on a zero-offset dataset, which contains both vertical and lateral heterogeneity and a total of nine point diffractors. Figure 6(a) shows the 7452 automatically picked data points plotted onto the coherence section obtained during the CRS attribute analysis. The event tags, which could be assigned successfully to each diffraction in an automated fashion (Bauer et al., 2019), are displayed in Figure 6(b), where each diffraction has a distinct color. As in the previous example, we applied both conventional wavefront tomography and diffraction wavefront tomography with and without using curvature information. For all inversion runs, we used an initial grid of 11×6 B-spline knots with a spacing of 1000 m each, which was halved three times during each inversion, thus ending up with a 81×41 grid with a spacing of 125 m each. The initial model of conventional wavefront tomography, for which again merely the near-surface velocity v_0 was assumed, is plotted in Figure 6(c) along with the initial localizations of all data points. Figure 6(d) shows the inverted model using the conventional scheme, in which the overall velocity distribution (compare Figure 6(h)) could be retrieved fairly well and the – independently treated – data points focus in the correct nine distinct subsurface regions. In

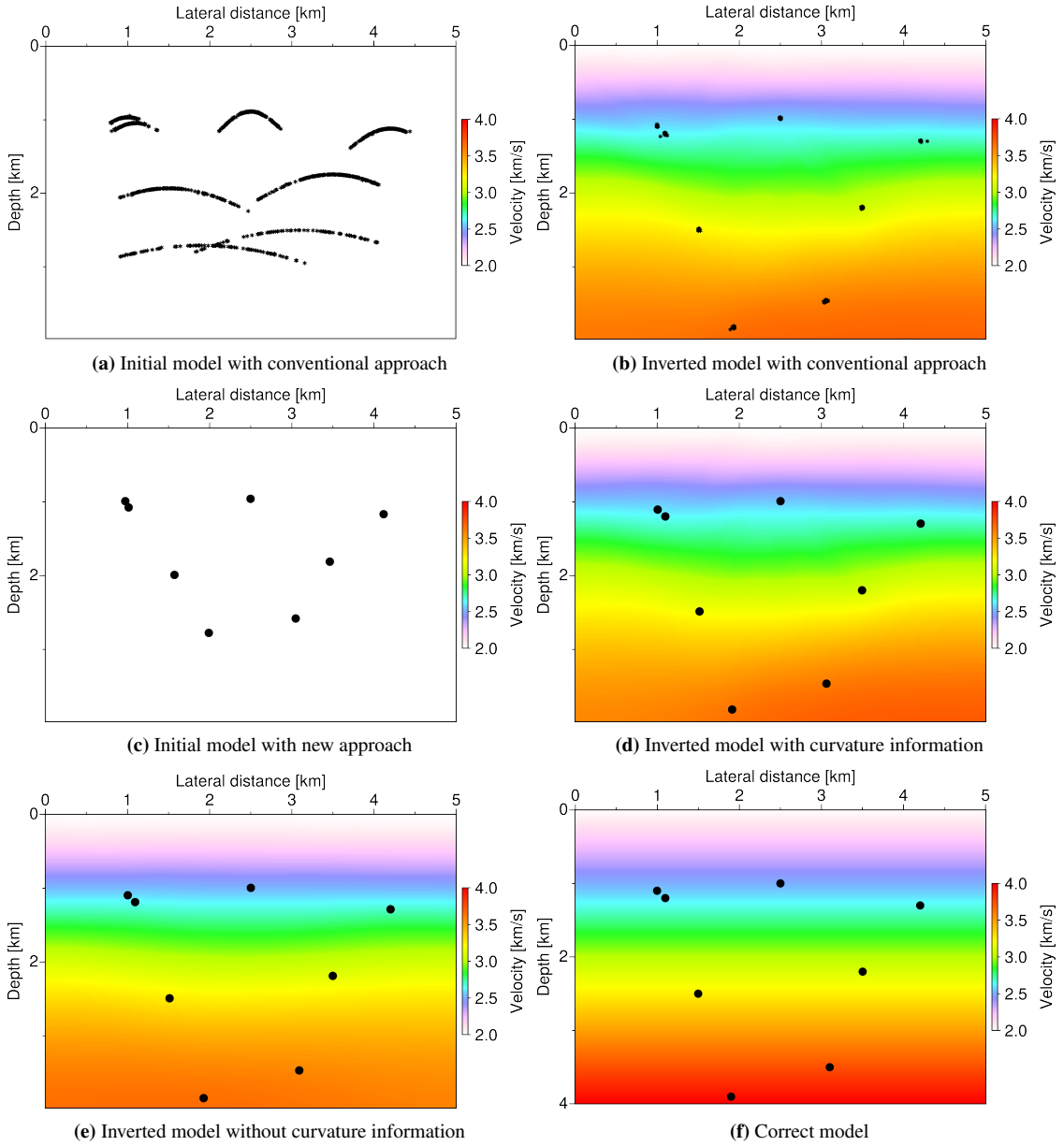

(a) Initial model with conventional approach

(b) Inverted model with conventional approach

(c) Initial model with new approach

(d) Inverted model with curvature information

(e) Inverted model without curvature information

(f) Correct model

Figure 5: Results for synthetic data with vertical heterogeneity: (a) the initial model with the initial localizations (black asterisks) using conventional wavefront tomography, (b) the inverted model with the conventional approach without enforced diffraction focusing with the final localizations (black asterisks), (c) the initial model of the new approach with the initial localizations (black dots), (d) the inverted model of the new approach obtained using curvature information with the final localizations, (e) the inverted model obtained without using curvature information with the final localizations, (f) the correct model with the correct diffractor positions.

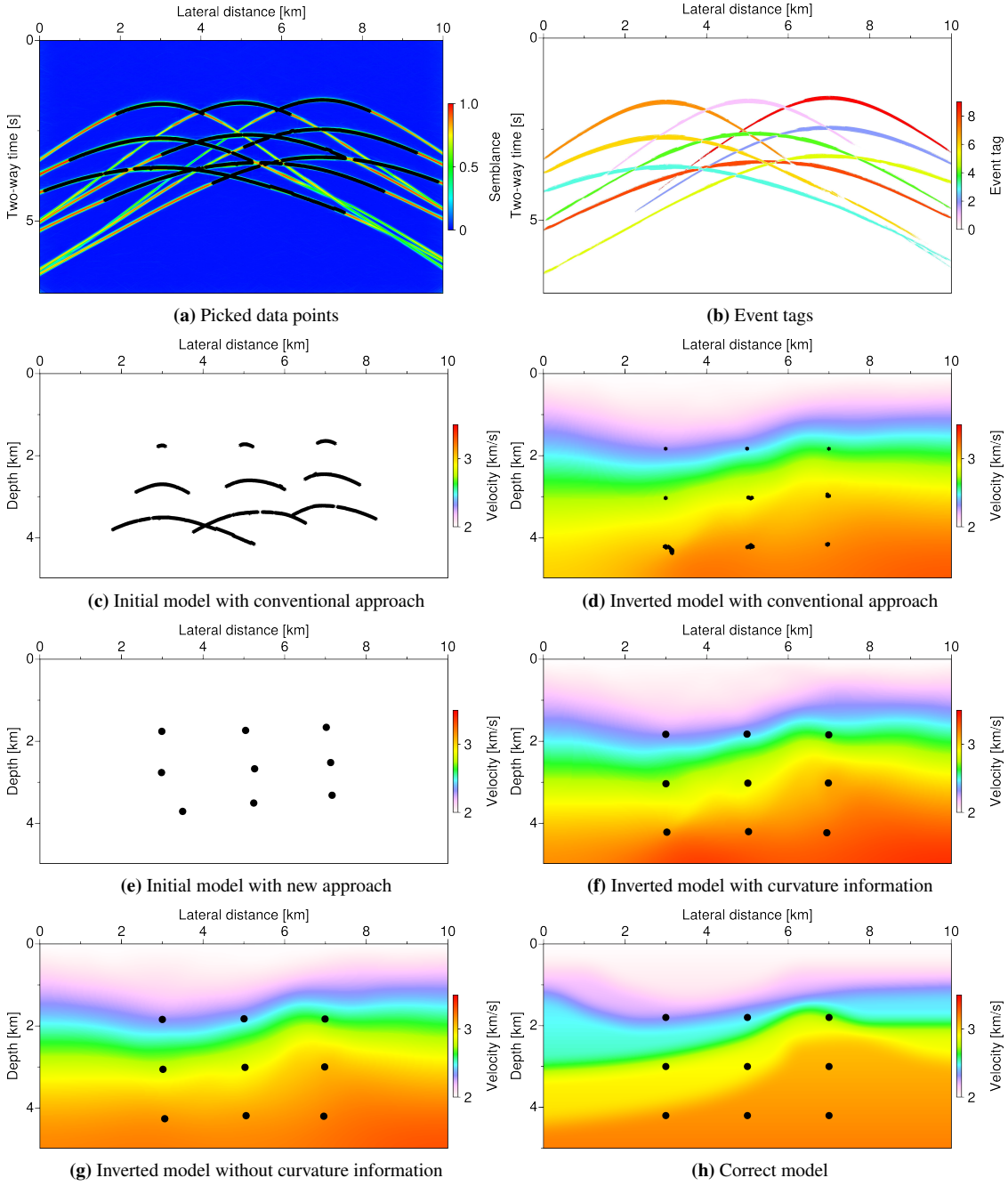

(a) Picked data points

(b) Event tags

(c) Initial model with conventional approach

(d) Inverted model with conventional approach

(e) Initial model with new approach

(f) Inverted model with curvature information

(g) Inverted model without curvature information

(h) Correct model

Figure 6: Results for synthetic data with vertical and lateral heterogeneity: (a) the picked data points (black asterisks) plotted into the zero-offset semblance section, (b) the event tags, (c) the initial model with the initial localizations (black asterisks) of conventional wavefront tomography, (d) the conventional inverted model with the final localizations, (e) the initial model with the initial localizations (black dots) of the modified approach, (f) the inverted model obtained using curvature information with the final localizations, (g) the inverted model obtained without using curvature information with the final localizations, (h) the correct model with the correct diffractor positions.

diffraction wavefront tomography, the data points connected to each event are not treated independently anymore, which leads to the initial localizations plotted in Figure 6(e) as black dots onto the constant initial model. Figures 6(f) and 6(g) are the velocity models and localizations obtained with the modified implementation that enforces diffraction focusing. While in the first, curvature information was used, the latter was obtained by setting the curvature weight w_M to zero, that is, the second-order attributes were not taken into account during the inversion. A comparison to the correct model with the correct diffractor positions (Figure 6(h)) reveals that the result obtained without using curvature information is the one closest to the correct model. This observation leads to the assumption that an inversion algorithm relying on curvatures may become less stable in settings with considerable lateral heterogeneity. However, the unique properties of diffractions allow to overcome this issue by enforcing their focusing in depth. This finding is supported by the fact that the conventional implementation of wavefront tomography, whose initial misfit exclusively depends on curvatures, for this example only converges, if the weight of the regularization term is increased.

CONCLUSIONS

We have presented a modified implementation of wavefront tomography (Duveneck, 2004; Bauer et al., 2017), which makes use of the unique physical properties of diffractions by forcing all measurements belonging to one diffraction to focus in the same subsurface location. A requirement for the application of the modified implementation is the a priori knowledge, which measurements in the data belong to the same diffraction. Once these event tags (Bauer et al., 2019) are available, all data points with the same event tag are forced to focus in depth by calculating a mean subsurface location for each event and assigning it to the corresponding data points during the inversion. While the initial misfit of conventional wavefront tomography exclusively depends on second-order wavefront attributes, which can be difficult to determine in complex settings, the modified implementation relies primarily on zero-order and first-order attributes, whose estimation is generally more stable. As the new approach allows not to take into account second-order attributes it evolves into a zero-offset slope tomography for diffractions in this case. Results for synthetic diffraction data confirm the potential of our approach and suggest that it benefits from the improved stability in settings with lateral heterogeneity. Future work comprises further improvement of the event-tagging algorithm (Bauer et al., 2019), the application to field data and the extension to 3D. Owing to their focusing nature, it can be demonstrated that the method is likewise applicable to passive-seismic events (Diekmann et al., 2019).

ACKNOWLEDGMENTS

This work was supported by the Federal Ministry for Economic Affairs and Energy of Germany (BMWi, 03SX427B) and by the sponsors of the Wave Inversion Technology (WIT) consortium, Hamburg, Germany. Benjamin Schwarz is supported by a research fellowship of the German Research Foundation (DFG, SCHW 1870/1-1).

REFERENCES

Bauer, A., Schwarz, B., and Gajewski, D. (2016). Enhancement of prestack diffraction data and attributes using a traveltime decomposition approach. *Studia Geophysica et Geodaetica*, 60(3):471–486.

Bauer, A., Schwarz, B., and Gajewski, D. (2017). Utilizing diffractions in wavefront tomography. *Geophysics*, 82(2):R65–R73.

Bauer, A., Schwarz, B., Werner, T., and Gajewski, D. (2019). Unsupervised event identification and tagging for diffraction focusing. *Geophysical Journal International*, 217(3):2165–2176.

Baykulov, M. and Gajewski, D. (2009). Prestack seismic data enhancement with partial common-reflection-surface (CRS) stack. *Geophysics*, 74(3):V49–V58.

Billette, F. and Lambaré, G. (1998). Velocity macro-model estimation from seismic reflection data by stereotomography. *Geophysical Journal International*, 135(2):671–690.

Dell, S. and Gajewski, D. (2011). Common-reflection-surface-based workflow for diffraction imaging. *Geophysics*, 76(5):S187–S195.

Diekmann, L., Schwarz, B., Bauer, A., and Gajewski, D. (2019). Source localisation and joint velocity model building using wavefront attributes. *Geophysical Journal International*.

Duveneck, E. (2004). Velocity model estimation with data-derived wavefront attributes. *Geophysics*, 69(1):265–274.

Eisenberg-Klein, G., Prüßmann, J., Gierse, G., and Trappe, H. (2008). Noise reduction in 2D and 3D seismic imaging by the CRS method. *The Leading Edge*, 27(2):258–265.

Fomel, S., Landa, E., and Taner, M. T. (2007). Poststack velocity analysis by separation and imaging of seismic diffractions. *Geophysics*, 72(6):U89–U94.

Hubral, P. (1983). Computing true amplitude reflections in a laterally inhomogeneous earth. *Geophysics*, 48:1051–1062.

Jäger, R., Mann, J., Höcht, G., and Hubral, P. (2001). Common-reflection-surface stack: Image and attributes. *Geophysics*, 66:97–109.

Khaidukov, V., Landa, E., and Moser, T. J. (2004). Diffraction imaging by focusing-defocusing: An outlook on seismic superresolution. *Geophysics*, 69(6):1478–1490.

Klokov, A. and Fomel, S. (2012). Separation and imaging of seismic diffractions using migrated dip-angle gathers. *Geophysics*, 77(6):S131–S143.

Krey, T. (1952). The significance of diffraction in the investigation of faults. *Geophysics*, 17(4):843–858.

Landa, E. and Keydar, S. (1998). Seismic monitoring of diffraction images for detection of local heterogeneities. *Geophysics*, 63(3):1093–1100.

Moser, T. J. and Howard, C. B. (2008). Diffraction imaging in depth. *Geophysical Prospecting*, 56(5):627–641.

Paige, C. C. and Saunders, M. A. (1982). LSQR: An algorithm for sparse linear equations and sparse least squares. *ACM Transactions on Mathematical Software (TOMS)*, 8(1):43–71.

Schwarz, B. (2019). Coherent wavefield subtraction for diffraction separation. *Geophysics*, 84(3):1–47.

Schwarz, B., Bauer, A., and Gajewski, D. (2016). Passive seismic source localization via common-reflection-surface attributes. *Studia Geophysica et Geodaetica*, 60(3):531–546.

Schwarz, B. and Gajewski, D. (2017). A generalized view on normal moveout. *Geophysics*, 82(5):V335–V349.

Tavakoli F, B., Operto, S., Ribodetti, A., and Virieux, J. (2017). Slope tomography based on eikonal solvers and the adjoint-state method. *Geophysical Journal International*, 209(3):1629–1647.

Virieux, J. and Operto, S. (2009). An overview of full-waveform inversion in exploration geophysics. *Geophysics*, 74(6):WCC1–WCC26.

Walda, J. and Gajewski, D. (2017). Determination of wavefront attributes by differential evolution in the presence of conflicting dips. *Geophysics*, 82(4):V229–V239.